PCCP

Effects of Dilution in Ionic Liquid Supercapacitors

Journal:	*Physical Chemistry Chemical Physics*
Manuscript ID	CP-ART-07-2022-003398.R1
Article Type:	Paper
Date Submitted by the Author:	11-Oct-2022
Complete List of Authors:	Varner, Samuel; California Institute of Technology, Division of Chemistry and Chemical Engineering Wang, Zhen-Gang; California Institute of Technology Division of Chemistry and Chemical Engineering,

PCCP

ARTICLE TYPE

Cite this: DOI: 00.0000/xxxxxxxxxx

Effects of Dilution in Ionic Liquid Supercapacitors†

Samuel Varner and Zhen-Gang Wang*

Received Date
Accepted Date

DOI: 00.0000/xxxxxxxxxx

Room-temperature ionic liquids (RTILs) are synthetic electrolytes that have a large electrochemical stability window, making them attractive candidates for electric double-layer capacitor (EDLC) applications. Due to their high viscosities and low ionic conductivities, RTILs are often diluted with organic solvent for practical use. We study the effects of dilution on the performance of RTIL EDLCs using a simple mean-field model. We find that dilution diminishes the unfavorable hysteresis that results from a spontaneous surface charge separation (SSCS). As a result, the RTIL concentration can be used to modulate the proximity to the SSCS transition, and maximize capacitance. The interplay between the concentration and the correlation strength gives rise to complex zero-potential phase behavior, including a tricritical point and a λ-line, very similar to the Blume–Capel dilute Ising model. Additionally, electrodes that are solvophilic aid in the prevention of SSCS by drawing solvent molecules to the electrode and displacing ions. Solvophilic electrodes give rise to a phase transition at finite potential where the surface charge rapidly increases with a small increase in potential, leading to a substantial increase in capacitance and energy storage.

Introduction

Electric double-layer capacitors (EDLCs), a subset of supercapacitors (SCs), are devices that store charge in an electric double-layer within an electrolyte near charged electrodes. EDLCs are extensively studied because they may have the capability to match the power density (PD) of traditional capacitors with the energy density (ED) of batteries.[1–3] When an electric field is applied between two electrodes, the formation of the double-layer is very rapid due to high ion mobility, especially for electrolytes with low bulk resistance (high ionic conductivity). This makes them useful for applications that require high cyclability and power delivery, such as in regenerative braking for electric vehicles.[4].

Since the maximum energy that can be stored by an EDLC scales as $CV^2/2$ (for constant C), increasing the cell potential V is a very effective way to improve EDLC devices.[5] The cell potential is determined by the electrolyte material being used, which can range from aqueous electrolytes and polyelectrolytes to organic electrolytes and even ionic liquids (ILs).[6] Both the PD and ED are greatly improved if the cell potential of the EDLC can be increased, *ceteris paribus*. Aqueous electrolytes remain electrochemically stable up to ~1 V, whereas organic replacements such as acetonitrile (AN) and propylene carbonate (PC) have wider potential windows up to ~2.5 V.[7] More recently, ILs are being studied as electrolytes for EDLCs due to their low volatility, high potential window and improved electrochemical stability.[1,5,8]

Room temperature ionic liquids (RTILs) are a special class of ILs that differ from traditional molten salts in many ways. A neat RTIL is typically made up of a bulky organic cation (e.g. imidazolium, pyrrolidinium, phosphonium) and a weakly coordinated organic/inorganic anion (e.g. tetrafluoroborate, trifluoromethanesulfonate, trifluoromethanesulfonimide).[5,9] Due to the organic and bulky nature of the ions, RTILs can exist as liquids at room temperature despite strong Coulomb interactions. Additionally, RTILs are non-volatile and can remain stable up to ~5 V, making them much more stable than aqueous and organic electrolytes. Their desirable properties make them prime candidates as electrolytes in EDLCs.[10–12]

For practical application of RTILs in EDLCs, it is crucial to understand the structure and behavior of the electric double-layer (EDL). The capacitance and energy storage are directly determined by the response of the EDL to applied potentials. The study of EDL structure goes back to Helmholtz in 1853.[13] At that time the EDL was described as a single layer of ions adjacent to a charged electrode which yielded a constant capacitance at all potentials. Now, more sophisticated theories incorporate physics like electrostatic correlation, non-electrostatic interactions and finite ion size.[14–21] The advent of more advanced theories was motivated by the discovery that electrostatic correlation and finite size effects are essential to the EDL behavior of RTILs.[22–24] Kornyshev[15] studied the finite size effects using a mean-field lattice-

Division of Chemistry and Chemical Engineering, California Institute of Technology, Pasadena, California, 91125, USA. E-mail: zgw@caltech.edu; Tel: +1 (626) 395-4647

† Electronic supplementary information (ESI) available: See DOI: 10.1039/cXCP00000x/

gas model with only single-occupation sites. The effect of ion crowding near the electrode with increasing potential gave a bell-shaped capacitance–potential curve, rather than the typical U-shaped curve that was predicted by Helmholtz. More interestingly, Kornyshev also discovered that there is a transition from bell-shaped to camel-shaped capacitance curves when the void space in the system was high enough, specifically for an ion volume fraction of $\gamma < 1/3$.

The Kornyshev model was then extended by Bazant–Storey–Kornyshev (BSK) to allow for electrostatic correlation phenomenologically via the incorporation of a non-local relative permittivity.[16] It was shown that short-ranged electrostatic correlations in neat RTILs can lead to overscreening, where the surface charge is overscreened in subsequent layers, leading to an oscillatory charge density profile that decays to the bulk value away from the electrode. This oscillatory behavior has been observed experimentally and in simulations of dense electrolytes such as RTILs where short-ranged electrostatic correlations are expected to be important.[25–27]. While the BSK model was successful at incorporating electrostatic correlations, the model was restricted to a fixed correlation strength, and did not incorporate dilution effects. The non-local relative permittivity introduced in the BSK model maps to a composite Coulomb–Yukawa potential, $U(r) = (1-\mathrm{e}^{-r/\ell_c})/4\pi\lambda_D^2 r$, where the Yukawa potential incorporates the short-ranged electrostatic correlations and non-electrostatic interactions.[28,29] Here ℓ_c is the correlation length, λ_D is the Debye length, and r is the interparticle distance. The BSK model was further expanded upon by allowing for the correlation strength to vary with the parameter α, $U(r) = (1-\alpha\mathrm{e}^{-r/\ell_c})/4\pi\lambda_D^2 r$.[18,30,31]. The correlation strength α incorporates the strength of electrostatic correlations as well as short-ranged non-electrostatic interactions between the bulky ions of RTILs. Caetano et al. first used this model to describe hydration mediated interactions in aqueous electrolytes.[17] The observed hysteresis in RTIL EDLCs[32,33] was first explained by Limmer as a result of a fluctuation induced first-order surface phase transition.[34] This spontaneous surface charge separation (SSCS) was also predicted using the composite Coulomb–Yukawa potential with a correlation strength above a critical value $\alpha > \alpha_{s,c}$.[18,30] The symmetry breaking transition is made possible by the short-ranged attraction of co-ions resulting from non-electrostatic (dispersion) interactions. Typically, in an inorganic electrolyte with small ions, the Coulomb repulsion would prevent the coions from coalescing at an electrode without a driving force. In the case of ILs, short-ranged dispersion forces offset the Coulomb repulsion and allow coions to gather at an electrode, inducing a surface charge. The result is a stable double layer formed spontaneously through ion density fluctuations and surface polarization. The image charge interactions are crucial for the surface transition. Recent coarse-grained molecular dynamics simulations show that SSCS is possible only with attractive image charges from a metal electrode.[35] The discussed mean-field theories (MFTs) do not distinguish the electrode type.

While there have been many studies about neat RTILs near electrified interfaces, there has been little work on diluted RTILs with account for finite size and electrostatic correlation, and little discussion on their capacitance and energy storage behavior. The high viscosity of RTILs at room temperature causes a low ionic conductivity and thus low PD.[7,36] High bulk resistance gives rise to slow charging/discharging dynamics. This is one of the main issues faced when using RTILs as the electrolyte for EDLCs. The most popular way to get around the high viscosity is by using mixtures of ILs and organic solvents, such as AN.[37–39] While the addition of organic solvents generally decreases the cell potential, exploratory studies have discovered RTIL–solvent mixtures that maintain a cell potential above 3V with high cyclability.[12,39] In most commercial applications, RTILs are diluted with AN or PC to achieve acceptable power delivery.[36] Incorporating neutral solvent into existing theories of RTIL EDLCs is crucial to more accurately model real systems and predict trends in ED and PD.

In this work, we further analyze the MFT used in recent works[30,31] by incorporating a neutral solvent. We investigate the effect of dilution on SSCS, capacitance, and energy storage for a single plate system. We also investigate the effects of preferential adsorption of solvent on the phase behavior, capacitance, and energy storage.

Model and Theory

The MFT is similar to that developed earlier[17] to describe hydration mediated interactions in dilute electrolyte where a Yukawa potential was used to account for correlations, and the Bikerman mixing entropy was used to account for finite ion size.[40] The model was more recently used to study the thermodynamic stability of neat ionic liquids and the spontaneous surface phase transition arising from ion–ion correlations.[18,30,31] These theories, however, have not yet been used to study the thermodynamic stability of diluted ionic liquids and the capacitance behavior in the charge separated regime. Briefly, a planar electrode is immersed in a size-symmetric 1:1 diluted RTIL where each ion carries unit charge $\pm e$ and has volume v and we define $b = v^{1/3}$ as the length scale of the ion. For simplicity, we assume the solvent also has molecular volume v. In the framework of the lattice-gas-like model, v corresponds to the volume of a lattice site where each lattice site can be occupied by a single particle. In principle, ion size asymmetry could be accounted for either phenomenologically as was done by Kornyshev,[15] or in an asymmetric lattice gas model as done by Han et al which uses a Flory–Huggins entropy.[41] We focus on the symmetric case in order to study the effects of dilution and ion–ion correlations. The dielectric constant of the RTIL is ε. The bulk ion volume fractions are $\phi_\pm^B = vc_\pm^B$ where c_i^B is the bulk number density of species i. A neat RTIL corresponds to $\phi_+^B = \phi_-^B = 1/2$. The solvent volume fraction is given by the incompressibility condition $\phi_s^B = 1 - \phi_+^B - \phi_-^B$. We use the B superscript to denote bulk values, while the inhomogeneous system profiles are denoted $\phi_+ = \phi_+(\mathbf{r})$, $\phi_- = \phi_-(\mathbf{r})$ and $\phi_s = \phi_s(\mathbf{r}) = 1 - \phi_+ - \phi_-$. The electrode carries surface charge σ while the system remains charge neutral.

We start with the modified BSK equation[16,17,31,42] with the ad-

dition of the chemical potential in the grand canonical ensemble,

$$\begin{aligned}\beta\Omega = &\int d\mathbf{r}\left[\phi_+\ln\phi_+ + \phi_-\ln\phi_- + (1-\phi_+-\phi_-)\ln(1-\phi_+-\phi_-)\right]\\ &+\frac{1}{8\pi\lambda_0^2}\int d\mathbf{r}\int d\mathbf{r}\frac{\phi(\mathbf{r})\phi(\mathbf{r}')}{|\mathbf{r}-\mathbf{r}'|}\\ &-\frac{\alpha}{8\pi\lambda_0^2}\int d\mathbf{r}\int d\mathbf{r}'\frac{\phi(\mathbf{r})\mathrm{e}^{-\frac{|\mathbf{r}-\mathbf{r}'|}{\ell_c}}\phi(\mathbf{r}')}{|\mathbf{r}-\mathbf{r}'|}\\ &-\int d\mathbf{r}_{||}\int dz\left[H_+(z)\phi_+(\mathbf{r})+H_-(z)\phi_-(\mathbf{r})\right]\\ &-\int d\mathbf{r}\left[\mu_+\phi_+(\mathbf{r})+\mu_-\phi_-(\mathbf{r})\right] \qquad (1)\end{aligned}$$

where the integration dimensions are normalized by the ion size b. The first integral is the translational entropy of the mixture proposed by Bikerman[40] with the incompressibility condition enforced. This is the most widely used model to account for finite ion size in MFTs of ionic liquids.[15–18,30,31] We drop the explicit notation for spatial dependence as it is understood that these profiles can be inhomogeneous. The second term is the coulombic interactions where $\phi=\phi_+-\phi_-$ is the local dimensionless charge density. The nondimensionalized nominal screening length is given by $\lambda_0=[\varepsilon_r\varepsilon_0 b/\beta e^2]^{1/2}$ with $\beta=1/k_BT$, elementary charge e, temperature T, Boltzmann constant k_B, vacuum permittivity ε_0, and relative permittivity ε_r. The third term is a Yukawa potential which accounts for the ion–ion correlations and the non-electrostatic interactions between the bulky organic ions, with α controlling the strength and the correlation length ℓ_c controlling the range. In principle, as shown by de Souza and Bazant[42], α and ℓ_c will vary with concentration; however, we assume they are independent and choose a particular section of the parameter space to explore. One could expand the model to include more chemical specificity by using a different α and ℓ_c for each pair of species.[30] Alternatively a Flory χ could be included between each species pair which is a much simpler local interaction that would still allow for chemical specificity.[43] The fourth term models the preferential adsorption/desorption of ions with the electrode, where $\mathbf{r}_{||}$ is the 2-dimensional position in the directions parallel to the electrode, z is position normal to the electrode, and $H_\pm$ are the adsorption potentials for the ions relative to the solvent. Note that the adsorption potentials $H_\pm(z)$ only depend on position normal to the surface, z. The last term contains the contributions from the chemical potentials μ_+ and μ_- where the solvent term is eliminated using the incompressibility condition. The system is grand canonical as it is connected to a bulk reservoir at fixed species chemical potentials.

For the single plate geometry, assuming the transverse directions are vast compared to the normal direction, we can reduce the model to a one-dimensional system. Instead of the vector position, $\mathbf{r}$, dependence is reduced to the coordinate z normal to the electrode face (normalized by b). Since the single-plate system is semi-infinite, we introduce a second plate at a sufficiently large distance L from the first plate to simplify numerical calculations. The two plates have the same magnitude of surface charge σ with opposite sign, and are located at $z=\pm L/2$. They are far enough that a significant region centered at $z=0$ is at the bulk condition of $\phi_\pm=\phi_\pm^B$.

The Coulomb term, the second term in Eq. (1) can be rewritten identically using an identity transform for quadratic interactions.[44,45] This introduces the nondimensional electrostatic potential $\psi=\beta e\Psi$ that is coupled to the mean charge density, ϕ. We also include preferential adsorption potentials to account for non-electrostatic electrode–electrolyte interactions.[18] The nondimensional grand free energy per unit area for the single plate system is

$$\begin{aligned}\frac{\beta\Omega}{A} = &\int_{-L/2}^{L/2} dz\left[\phi_+\ln\phi_+ + \phi_-\ln\phi_- + (1-\phi_+-\phi_-)\ln(1-\phi_+-\phi_-)\right]\\ &+\int_{-L/2}^{L/2} dz\left\{\left[\phi+\sigma\delta\left(z+\frac{L}{2}\right)-\sigma\delta\left(z-\frac{L}{2}\right)\right]\psi-\frac{\lambda_0^2}{2}\left|\frac{\partial\psi}{\partial z}\right|^2\right\}\\ &+\frac{\alpha}{2\lambda_0^2}\int_{-L/2}^{L/2} dz\int_{-L/2}^{L/2} dz'\,U(z-z')\phi(z)\phi(z')\\ &-\int_{-L/2}^{L/2} dz\left[H_+\phi_+ + H_-\phi_-\right]\\ &-\int_{-L/2}^{L/2} dz\left[\mu_+\phi_+ + \mu_-\phi_-\right] \qquad (2)\end{aligned}$$

where the Yukawa potential is $U(z-z')=-\frac{\ell_c}{2}\mathrm{e}^{-|z-z'|/\ell_c}$ and A is the electrode area. The fourth term accounts for the preferential adsorption/desorption of ions and solvent. The solvent contribution is eliminated from this term using the incompressibility condition. We use the same short-ranged preferential adsorption potential that was used by Chao and Wang (CW) in their study of preferential adsorption of ionic liquids.[18] This form was invoked for numerical stability and to maintain consistency with the length scale of the RTIL, b. In principle the potential could be a delta function at each surface, rather than be position dependent. We choose to use a smooth potential for numerical stability.

$$H_\pm(z)=\begin{cases}(1-z-\frac{L}{2})^2\Delta h_\pm & -L/2\le z<-L/2+1\\ 0 & -L/2+1\le z<L/2-1\\ (1+z-\frac{L}{2})^2\Delta h_\pm & L/2-1\le z\le L/2\end{cases} \qquad (3)$$

where strength of the harmonic adsorption for each ion type relative to the solvent is denoted $\Delta h_\pm=h_\pm-h_s$.[18] In general, the strength of the interaction can be different for cations and anions. However, for simplicity, we assume that $\Delta h=\Delta h_+=\Delta h_-$, and therefore $H=H_+=H_-$. Note, the negative sign in front of the adsorption term of eqn (2) means that when Δh is negative, the electrode has a higher affinity for the solvent than the ions.

Setting the variation of the free energy Ω with respect to ψ and

$\phi_\pm$ to zero, we obtain the following set of self-consistent equations

$$-\lambda_0^2 \frac{\partial^2 \psi}{\partial z^2} = \phi + \sigma\delta\left(z+\frac{L}{2}\right) - \sigma\delta\left(z-\frac{L}{2}\right) \tag{4}$$

$$\ln\left(\frac{\phi_+}{1-\phi_+-\phi_+}\right) + \psi + Y - H_+ - \mu_+ = 0 \tag{5}$$

$$\ln\left(\frac{\phi_-}{1-\phi_+-\phi_-}\right) - \psi - Y - H_- - \mu_- = 0 \tag{6}$$

where we have introduced the Yukawa field Y defined by the convolutional integral

$$Y(z) = \frac{\alpha}{\lambda_0^2}\int_{-L/2}^{L/2} dz' U(z-z')\phi(z') \tag{7}$$

Since the system is symmetric, we have the condition $\partial_z\psi|_{z=0} = 0$. Integrating over the domain and noting that inside the electrodes $\partial_z\psi = 0$ yield the boundary conditions

$$-\lambda_0^2 \left.\frac{\partial \psi}{\partial z}\right|_{z=\pm L/2} = \sigma \tag{8}$$

The Poisson equation, eqn (4), can be solved efficiently via finite difference, or can be solved via direct integration

$$\psi(z) = \psi(0) - \frac{1}{\lambda_0^2}\int_0^z dz'(z-z')\phi(z') \tag{9}$$

where $\psi(0) = 0$ for the symmetric two-plate system. Although one can obtain $Y(z)$ in terms of $\phi(z)$ using the integral form of eqn (7), computationally it is more convenient to solve for $Y(z)$ from a differential equation. To this end, differentiating eqn (7) twice yields

$$\frac{\partial^2 Y}{\partial z^2} - \frac{Y}{\ell_c^2} = \frac{\alpha}{\lambda_0^2}\phi(z) \tag{10}$$

Differentiating eqn (7) once and setting $z = 0$ yields the boundary condition

$$\left.\frac{\partial Y}{\partial z}\right|_{z=\pm L/2} = \mp\frac{Y(\pm L/2)}{\ell_c} \tag{11}$$

which agrees with previously obtained results[30,31] for no Yukawa source at the electrode. Assuming the bulk is a homogeneous 1:1 ionic liquid with ion volume fractions $\phi_\pm^B = \phi^B$, we may set $\psi = Y = H = \phi = 0$. Using the bulk conditions in addition to the equilibrium conditions $\mu_+ = \mu_+^B$ and $\mu_- = \mu_-^B$, we obtain an equation for the chemical potential.

$$\mu = \mu_+ = \mu_- = \ln\left(\frac{\phi^B}{1-2\phi^B}\right) \tag{12}$$

Inserting eqn (12) into eqn (5) and eqn (6) gives equations for the ion density profiles in terms of the potentials ψ, Y, and H,

$$\phi_+ = \frac{e^{-(\psi+Y)}}{(1/\phi^B - 2)e^{-H} + 2\cosh(\psi+Y)} \tag{13}$$

$$\phi_- = \frac{e^{\psi+Y}}{(1/\phi^B - 2)e^{-H} + 2\cosh(\psi+Y)} \tag{14}$$

Equations (4), (10), (13) and (14), along with boundary conditions in eqn (8) and eqn (11) constitute a set of self-consistent equations which can be solved iteratively with an initial guess for $\phi(z)$. For all calculations we set $T = 300\,\mathrm{K}$ and $b = 1\,\mathrm{nm}$. BSK predicted that the correlation length is on the order of the molecular size; therefore, we set $\ell_c = v^{1/3}$.[16] We choose $\varepsilon_r = 10$ in accordance with experimental measurements of imidazolium-based ionic liquids.[46] These values result in a nominal screening length of $\lambda_0 = 0.12$.

Zero applied field

For the case of no applied potential, the electrostatic potential difference between the two separated plates is zero, $\Delta V = \psi_{-L/2} - \psi_{L/2} = 0$. The mean-field equations are solved self-consistently via the following algorithm. An initial guess is made for $\phi(z)$. $\psi(z)$ is calculated from eqn (4) with the boundary conditions in eqn (8). $Y(z)$ is calculated from eqn (10) with the boundary condition given in eqn (11), and $H(z)$ is calculated from eqn (3). ψ, Y, and H are used in eqn (13) and eqn (14) to calculate new profiles ϕ_+ and ϕ_-, and therefore $\phi(z) = \phi_+ - \phi_-$. This process is repeated until the maximum difference in local charge density between subsequent iterations is below a tolerance, set to 10^{-10} for our calculations.

Applied field

In the case of an applied field, $\psi_{-L/2} = -\psi_{L/2} \neq 0$ and we specify the surface charge on the left and right plate to be σ and $-\sigma$ respectively. For each σ, we calculate the equilibrium profiles and extract the surface potential on each plate, which effectively yields the relationship $\sigma(\Delta V)$, where ΔV is the difference in surface potential between the two plates. The differential capacitance is calculated as

$$C_{\mathrm{diff}} = \frac{\partial|\sigma|}{\partial \Delta V} \tag{15}$$

and the energy storage per surface area is calculated as

$$\Delta F = \int_{\sigma(0)}^{\sigma(\Delta V)} u\, d\sigma = \int_0^{\Delta V} C u\, du \tag{16}$$

where σ, ΔV, C_{diff} and ΔF are in units of e/b^2, k_BT/e, e^2/k_BTb^2 and k_BT/b^2 respectively.

Results and Discussion

Effect of dilution on spontaneous surface charge separation

We first study the effect of dilution on spontaneous surface charge separation when there is no applied potential, $\Delta V = 0$. We vary the Yukawa interaction strength from $\alpha = 0$ to $\alpha = 1$, and the bulk ion volume fraction from $\rho^B = \phi_+^B + \phi_-^B = 0.05$ to $\rho^B = 1$. It is expected that dilution should weaken the effect of correlations[31], making the critical correlation strength for SSCS, $\alpha_{s,c}$, larger. Thus, a neat RTIL that undergoes SSCS at a particular $\alpha_{s,c}$ may not undergo any SSCS after dilution. We can observe SSCS by varying the bulk ion concentration ρ^B at a fixed correlation strength α.

We find that when α is moderately above the transition value for neat IL SSCS, the transition density decreases, but the transition remains second-order. When α is well above the transition

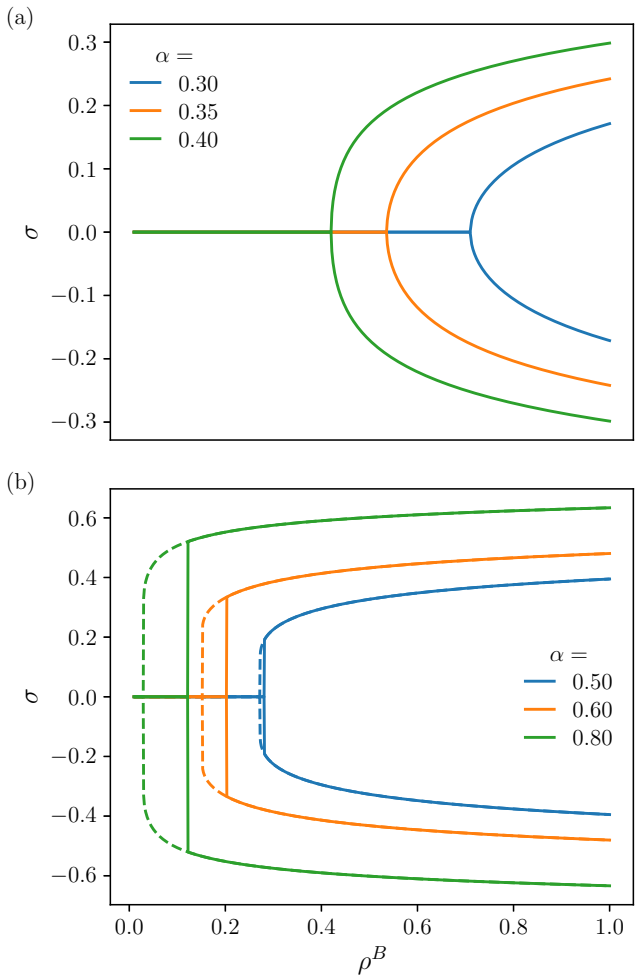

Fig. 1 (a) second-order SSCS transition, for a specified α, the transition occurs at a critical bulk ion concentration. Note, $\rho^B = \phi_+^B + \phi_-^B = 2\phi^B$ is the total ion concentration in the bulk. There are two branches because the symmetry can spontaneously break in either direction. (b) first-order SSCS transition, for a specified α, the transition occurs at different bulk ion concentrations depending on the initial state of the system, indicating metastability of the two phases. Solid lines correspond to paths taken starting from homogeneous states, whereas dashed lines correspond to paths taken starting from a charge-separated state. Vertical lines do not represent real trajectories, they are merely visual to guide the eye. The transition is discontinuous in the first-order region.

value for neat IL SSCS, the transition can happen at a lower density and the nature of the transition changes from second-order to first-order. Fig. 1 shows SSCS in systems with α moderately (a) and significantly (b) above the neat ionic liquid transition value of $\alpha_{s,c} = (\lambda_0/\ell_c)^2 + 2(\lambda_0/\ell_c) = 0.25$ for $\lambda_0/\ell_c = 0.12$.[31]. Fig. 1a shows a second-order transition in the surface charge density with increasing ρ^B while Fig. 1b shows a first-order transition. Additionally, as conjectured in Ref. 31, stronger correlations lead to a lower transition density.

The first-order behavior is characterized by metastability. When starting from a charge separated state and slowly decreasing the bulk concentration, the charge separated state remains metastable until a lower ρ^B value than when starting from a homogeneous state and slowly increasing ρ^B, as shown in Fig. 1b. Furthermore, note that the surface charge no longer increases continuously from 0 upon SSCS. Instead, the surface charge jumps from 0 to a finite value at the disordered spinodal and similarly jumps from a finite value down to 0 at the ordered spinodal. The true equilibrium transition ρ^B value is determined by the equality of the grand free energy density between the two branches. See the ESI† for more information on determining the transition point. The grand free energy is obtained by using the converged profiles ψ, Y, and $\phi_\pm$.

Charge overscreening and crowding

SSCS is accompanied by the presence of decaying oscillatory charge density profiles away from a charged electrode. The overcompensation of surface charge and the resulting oscillatory charge density and electrostatic potential profiles have been described as *overcharging*, or *overscreening*.[16,27,47] This phenomenon has been well documented for dense ionic systems near charged surfaces. In the case of BSK, the surface is charged and the ionic liquid overcompensates the surface charge, whereas in our case the surface charge is generated by the spontaneous charge separation of the ionic liquid. In either case, *overscreening* of the charge occurs. An example of an oscillatory charge density profile for a neat RTIL is given in Fig. 2a. The oscillations become more pronounced as the correlation strength α increases.

For very strong correlations (e.g. $\alpha = 1.1$), the effects of lattice saturation, or *crowding*, are observed. For the red and green curves in Fig. 2a, the layer adjacent to the electrode extends out into the solution. This is a result of the finite size of the ions in the lattice-gas-like model. Since the charge density cannot exceed unity, as the driving force for separation increases, the counterion layer adjacent to the electrode grows.

As the RTIL is diluted, the effect of correlations decreases and the driving force for SSCS decreases with it. As a result, both *overscreening* and *crowding* should be diminished as the RTIL concentration decreases. Indeed this is shown in Fig. 2c. As the RTIL is diluted, the extent of overscreening is diminished until eventually SSCS no longer occurs.

Phase diagram for SSCS at zero potential

For neat RTILs, the CW model shows a second-order transition at a critical alpha value, $\alpha_{s,c}$, at zero potential ($\Delta V = 0$).[18] The spontaneous surface charge separation is similar to the spontaneous magnetization in the mean-field Ising model, where the surface charge is the analog of the magnetization.

It is of interest to determine the exact nature of the first-order and second-order behavior in the relevant parameter space. Specifically, what is the location of the tricritical point with respect to concentration (or μ) and correlation strength? To answer this question a phase diagram in $\alpha - \mu$ space was generated numerically. For a comprehensive description of the algorithm, see the ESI†.

As shown, dilution decreases the effects of SSCS, meaning that a dilute system will have a higher $\alpha_{s,c}$ than a neat RTIL. This can be easily understood since the neutral solvent increases the aver-

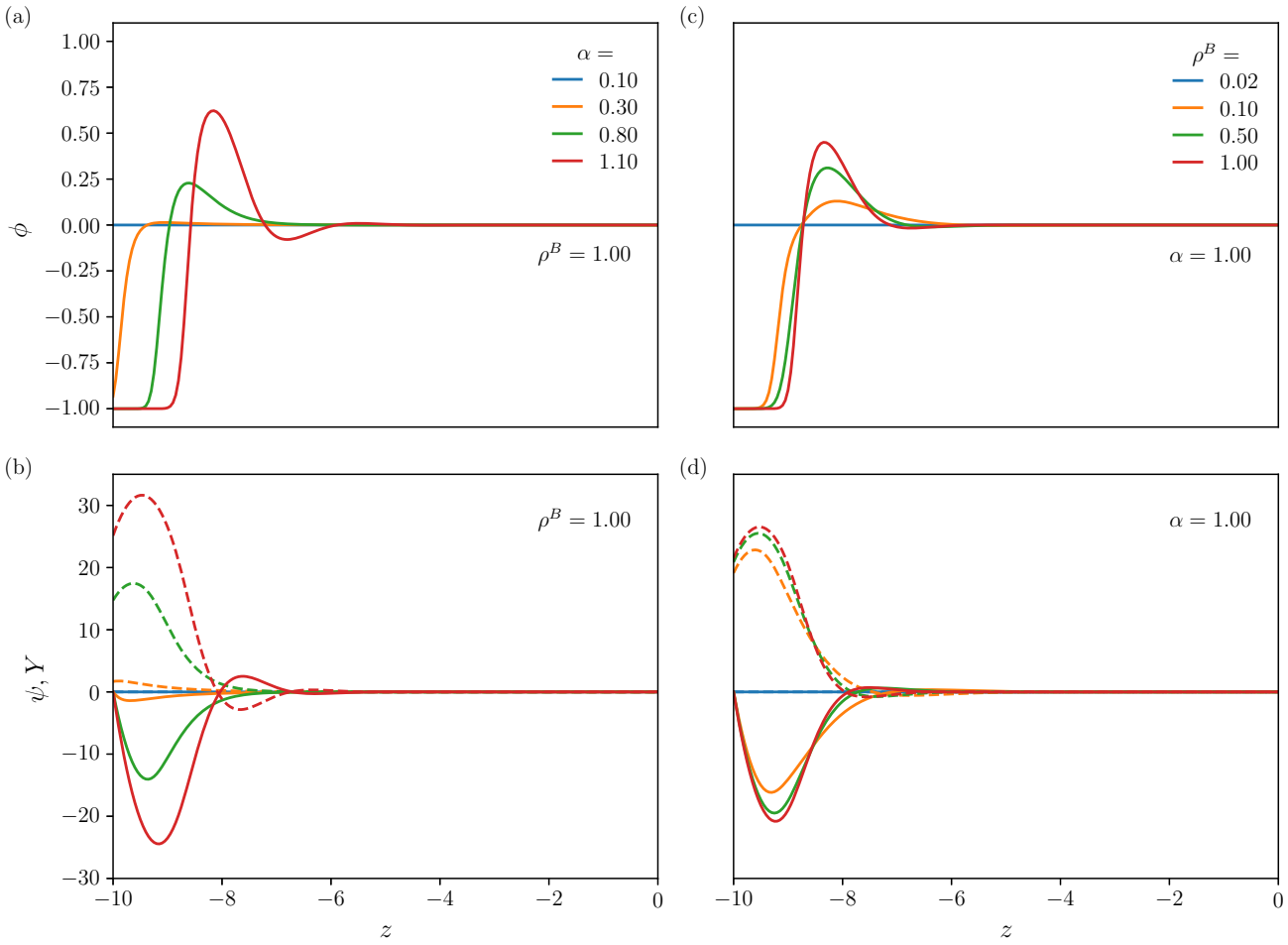

Fig. 2 (a) Charge density profiles near a positively charged electrode for a neat RTIL, $\rho^B = 1$. Profiles for various α are shown, all with $\Delta V = 0$. (b) Potential profiles corresponding to the charge density profiles in (a) where the electrostatic potential is given by solid lines and the Yukawa potential is given by dashed lines. (c) Charge density profiles near a positively charged electrode for a diluted RTIL with $\alpha = 1$ and $\Delta V = 0$. (d) Potential profiles corresponding to the charge density profiles in (c) where the electrostatic potential is given by solid lines and the Yukawa potential is given by dashed lines.

age distance between ions, reducing the effects of short-ranged correlations. The CW model shows that for neat RTILs the transition value is determined by $\alpha_{sc,neat} = 2\lambda_0/\ell_c + \lambda_0^2/\ell_c^2$.[31] For any dilute system, it should hold that $\alpha_{sc,dilute} > \alpha_{sc,neat}$. Thus, For any $\alpha < \alpha_{sc,neat}$ there will never be SSCS at any bulk ion density. This sets a lower bound for the value of α in the α–μ phase diagram.

The phase diagram in $\alpha - \mu$ space is given in Fig. 3. At the lower right part of the phase diagram, the SSCS transition is second-order as indicated by a line of critical points (the λ-line; the dashed green curve). For larger α and low bulk density, the transition becomes first-order indicated by the solid blue binodal, which is flanked by the spinodals of the disordered phase (solid black line) and the spinodal of the SSCS state (solid red line). The λ-line and the binodal meet at the tricritical point, where the two spinodal lines also terminate with a common tangent. The tricritical point occurs at $\mu = -\ln 4$ or $\rho_B = 1/3$. We note that this volume fraction is the same value that results in a transition from bell to camel-shaped capacitance curves, as shown by Kornyshev.[15] The transition in the shape of the capacitance curves occurs even without consideration of correlations and is a result of the finite ion size as treated with the lattice model. We see in the case of the diluted RTIL with correlations that the transition in the shape of the capacitance curve at critical dilution coincides with a transition in the phase behavior.

Beyond the mean-field, fluctuations will change the nature of the transition. It has been shown that the transition in concentrated ILs is weakly first-order rather than second-order, putting it in the Brazovski universality class.[34,48] Coarse-grained molecular dynamics simulations of neat RTILs also indicate a weakly first-order transition.[35]

Connection to Blume–Capel Model

The SSCS is a transition involving spontaneous symmetry breaking in the presence of a diluent. This is reminiscent of the spontaneous magnetization in the diluted Ising model, the spin-1 Ising model or the Blume–Capel (BC) model (a subset of the well known Blume–Emery–Griffiths model).[49–52] The BC/BEG model accurately captures the tricritical behavior of $He^4 - He^3$ mixtures,

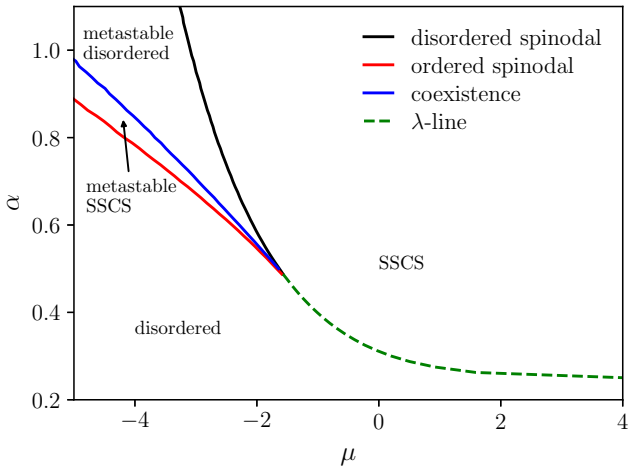

Fig. 3 RTIL SSCS phase diagram in $\alpha-\mu$ space. The dashed λ-line is a line of critical points where second-order transitions occur. The blue coexistence line and the black and red spinodals are a region of first-order transitions. The transition from second-order to first-order occurs at the *tricritical point*.

where the fluid-superfluid transition goes from second-order to first-order at a critical amount of He^3 impurity. The diluted RTIL shows a transition from second-order to first-order phase behavior below a certain ion concentration, where the neutral solvent plays the role of impurities. To show the comparison, we briefly derive results of the BC model.

The Hamiltonian of the BC model in the constrained grand canonical ensemble is given by,

$$H(\{\mathbf{s}\},N,T,\mu_A,\mu_B) = -\frac{J}{2}\sum_i\sum_j^{n.n.} s_i s_j - \Delta\mu\sum_i s_i^2 \qquad (17)$$

where s_i is the spin on particle i (±1 for interacting particles, A, and 0 for impurities, B), $J>0$ is the ferromagnetic interaction strength, and $\Delta\mu=\mu_A-\mu_B$ is the chemical potential difference between particle types. The sum over j is over the nearest neighbors of spin i.

We define the relative magnetization order parameter $m=\sum_i s_i/N_A$ and the type A spin concentration $x=N_A/N$ in order to write the mean-field Hamiltonian. The Gibbs Entropy is used with the mean-field Hamiltonian to write a variational free energy, $G=\langle H\rangle - TS$. The non-dimensional variational free energy per spin is

$$g=\frac{G}{Nk_BT} = -\frac{1}{2}\alpha x^2m^2-\mu x + x\frac{1+m}{2}\ln\left(x\frac{1+m}{2}\right)+$$
$$+x\frac{1-m}{2}\ln\left(x\frac{1-m}{2}\right)+(1-x)\ln(1-x) \qquad (18)$$

where $\alpha\equiv zJ/k_BT$, $\mu\equiv\Delta\mu/k_BT$, and z is the coordination number of the lattice. Minimizing the free energy gives the mean field equations

$$m=\tanh(\alpha x m) \qquad (19)$$

$$\mu=\ln\frac{x}{1-x}-\alpha x m^2+\frac{1+m}{2}\ln\frac{1+m}{2}+\frac{1-m}{2}\ln\frac{1-m}{2} \qquad (20)$$

which can be analyzed to obtain a phase diagram for the fluid-superfluid transition. The $\alpha-\mu$ phase diagram for the BC model has the same characteristic shape as the phase diagram for the dilute RTIL model in this study. We observe tricritical behavior

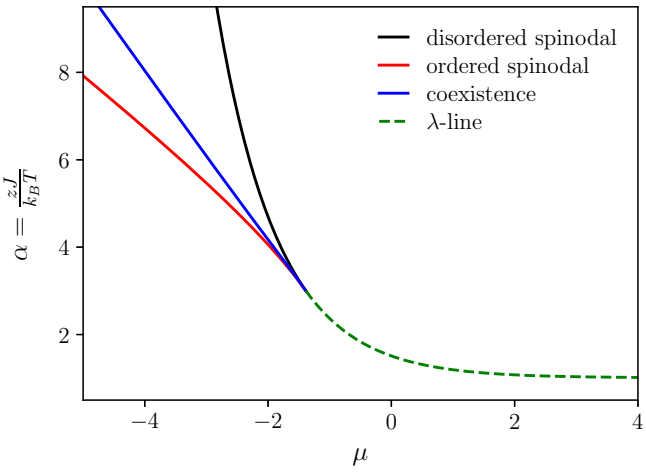

Fig. 4 $\alpha-\mu$ phase diagram for the mean-field BC model.

at the same chemical potential, which corresponds to $\mu=-\ln 4$ or $x=\rho^B=1/3$. Note, this is the same concentration, $\gamma=1/3$, discovered by Kornyshev[15] where the capacitance curve transitions from bell to camel-shaped. This analysis confirms the strong analogy between the currently studied dilute RTIL model and the *dilute Ising model*. The BC model and variants have also been used to study confined ionic liquids, and similar tricritical phase behavior is reported.[53,54] That the tricritical point for both the SSCS transition and the BC/BEG model occurs at $\rho=1/3$ is striking. However, the exact reason for this remains to be understood.

Capacitance and energy storage of dilute RTIL

Modulation of the distance to the $\alpha_{s,c}$ can be beneficial in multiple ways, first by preventing unwanted hysteresis in charging and discharging, but also by allowing for a large zero-potential capacitance. We have shown that addition of neutral solvent increases $\alpha_{s,c}$; here we discuss how this affects the capacitance and energy storage.

In order to see the effect of α in dilute systems, we first look at the $\alpha=0$ case that was studied by Kornyshev.[15]. He observed a transition from bell to camel-shaped capacitance curves at significant dilution.[15] The framework developed in our theory successfully reproduces the results of Kornyshev when $\alpha=0$, as shown in Fig. 3 in the ESI†. The transition from bell to camel-shaped curves occurs at $\rho^B=1/3$, as expected. While the zero-potential capacitance is lower for the dilute RTIL, at high potentials, the more dilute RTILs have higher capacitance. As pointed out by May[55], the

increase in capacitance with dilution at high potential comes from a frustration relief of the EDL, where coions near the surface are replaced by solvent molecules. Recent works have discovered a "bird-shaped" capacitance curve that occurs near the RTIL–solvent demixing transition when ionophilic electrodes are used.[56] While we did not observe this shape with the given model, we believe this shape can be achieved by adding a local repulsion between ions and solvent via a Flory χ parameter. Ionophilic electrodes can be modeled by setting Δh to a positive value. We leave this exploration for a future study.

With correlations accounted for in the Yukawa potential, dilution effectively raises $\alpha_{s,c}$. Figure 5a shows that hysteresis in charging/discharging can be minimized or even prevented via dilution. The $\sigma - \Delta V$ curve for $\rho_B = 1.0$ (purple) exhibits metastability where σ and ΔV have opposite signs, while the stability condition $\partial\sigma/\partial\Delta V > 0$ is still satisfied. There is also a region of instability indicated by a dashed line where $\partial\sigma/\partial\Delta V < 0$. For a given α, instability and metastability can be mitigated by diluting enough with a neutral solvent such that $\alpha \leq \alpha_{s,c}$. For $\alpha = 0.35$ we see that at the corresponding critical concentration of $\rho_B = 0.55$ the slope diverges at $\Delta V = 0$. See the red curve in Fig. 5a. This means that for an RTIL with $\alpha = 0.35$, one can maximize the zero-potential capacitance by diluting the RTIL down to 55% v/v. We again acknowledge that α for a given RTIL could generally depend on the ion concentration;[42] however, the extent and form of the dependence is not the focus of this study. Here, we assume that α is independent of the concentration and explore the parameter space.

Capacitance curves for $\alpha = 0.35$ are shown in Fig. 5b and c. The zero-potential capacitance first increases upon dilution (purple to red). The maximum capacitance is reach when the concentration is such that $\alpha = \alpha_{s,c}$. Further dilution results in a decrease in zero-potential capacitance (red to green to orange to blue) because it brings the system further below $\alpha_{s,c}$. For $\rho^B < 1/3$ the maximum in capacitance characteristic of the camel shaped capacitance curves is still present. Similarly, for high enough potentials, the capacitance increases with dilution due to EDL frustration relief.

Figure 6 show the zero-voltage capacitance as a function of ρ^B at different values of α. The capacitance diverges for a critical ρ^B value whose $\alpha_{s,c}$ becomes equivalent to α for the given RTIL.

Since dilution leads to a higher capacitance at high potentials, it is conceivable that the energy storage could be higher in more dilute RTILs at the same charging potential. The energy storage is calculated via eqn (16) and plotted in Fig. 7 for an RTIL with $\alpha = 0.35$. If the capacitor is charged to higher potentials, it is evident that more dilute RTILs can store more energy per unit area. This is because of the higher capacitance in dilute RTILs at high potential, which is shown in Fig. 5b and c. We see that even at the critical concentration of $\rho^B = 0.55$ where the zero-voltage capacitance diverges, the energy storage is relatively low. As explained by Chao and Wang[18], this is due to the peak in capacitance being counterbalanced by the zero of potential in the integral in eqn (16). In order to combat this, Chao and Wang proposed preferential adsorption where one ion is preferentially attracted to a particular electrode. The result was a shifted diverging capaci-

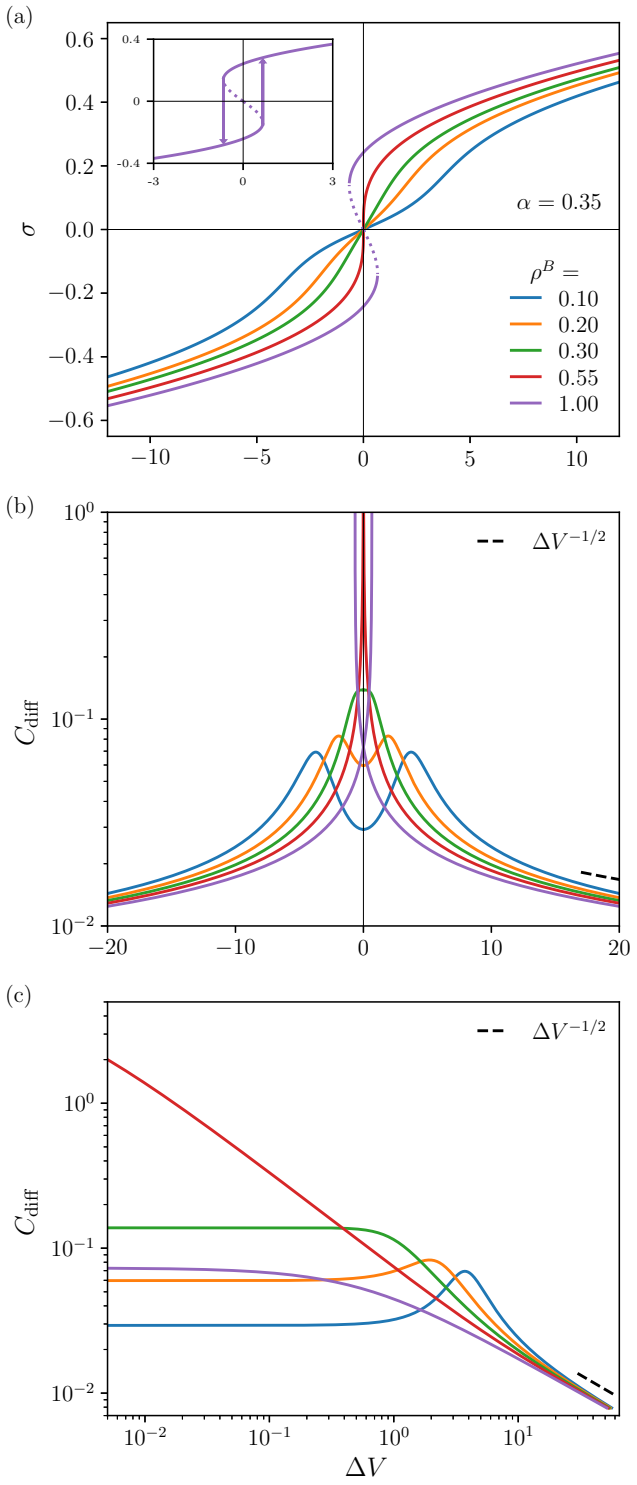

Fig. 5 (a) σ vs ΔV plotted for a RTILs with varying dilution and $\alpha = 0.35$. The dashed portion of $\rho_B = 1.0$ (purple) curve is the region of instability. The inset shows the $\rho_B = 1.0$ curve with arrows indicating the trajectory the system would follow when slowly charging or discharging. Starting on the bottom solid curve at -3 and increasing the voltage, the system becomes metastable once 0 is crossed. As the potential is increased further, the system may jump up to the positive branch. The arrow is located at the spinodal, where the system must jump to the stable positive branch. (b) and (c) C_{diff} vs ΔV plotted for RTILs with varying dilution on semi-log and log-log scales respectively. The capacitance curves are calculated using only the stable and metastable portions of the $\sigma - \Delta V$ curves. The legend in (a) applies to (b) and (c) as well.

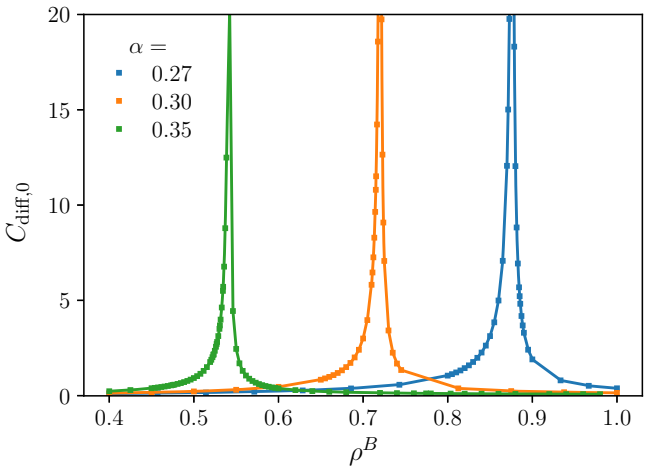

Fig. 6 $C_{\mathrm{diff}}(\Delta V = 0)$ vs ρ_B for different values of α. Note that α is below the value at the tricritical point, and therefore the transition remains second-order.

tance which leads to a substantial increase in energy storage. We would expect similar results with asymmetric ion adsorption in diluted RTILs, so we instead focus on solvent adsorption which is specific to our work.

Preferential adsorption of solvent

We assume the same short-ranged preferential adsorption for the solvent that has previously been used to describe preferential adsorption of ions in neat RTILs[18,31]. The form of the potential is given in eqn (3). We assume that the two ions have the same interaction with the electrodes while the solvent interaction differs. Under the assumption of indifferent adsorption between the cation and anion, the relevant interaction is the difference between the solvent and the ions with the surface. A negative Δh implies that the solvent is preferentially attracted to the electrode,

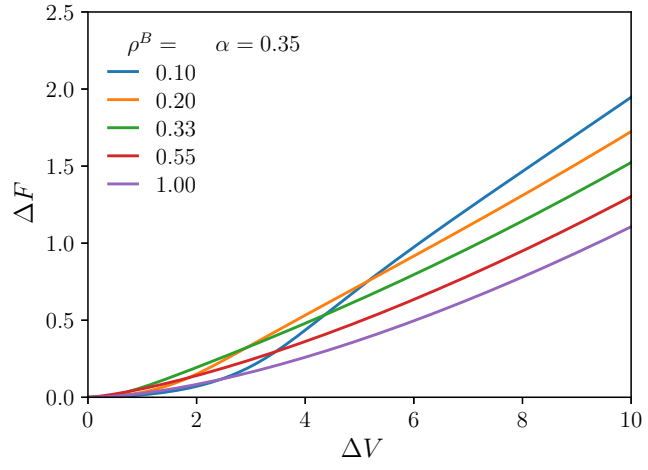

Fig. 7 Energy storage per unit area for an RTIL with $\alpha = 0.35$ at various levels of dilution.

or that the electrode is solvophilic. We expect that a solvophilic electrode will diminish unfavorable hysteresis and SSCS by drawing solvent to the electrode and pushing ions away. To study the SSCS behavior we set zero surface potential and vary the bulk ion concentration. The $\alpha - \mu$ phase diagram for a diluted RTIL with $\Delta h = -5$ is given in Fig. 8. The main effect on the zero-voltage behavior is that for a given chemical potential, a higher α is required to induce SSCS.

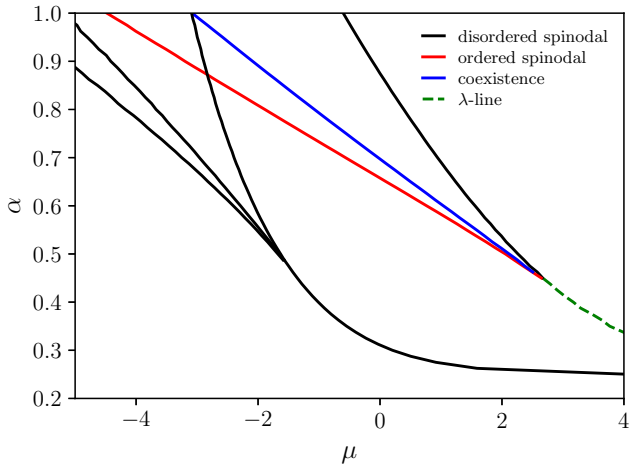

Fig. 8 $\alpha - \mu$ phase diagram for a dilute RTIL with a solvophilic electrode, $\Delta h = -5$. The black superimposed phase diagram is the result for no preferential adsorption.

Preferential adsorption of solvent repels ions away from the electrode. At low potential, this leads to a lower differential capacitance as the driving force for ions to replace the solvent molecules is low. As the potential increases, the system undergoes a surface transition where the solvent molecules are replaced with counterions. We note that this finite potential transition can occur in systems with no preferential adsorption, so long as the RTIL concentration is sufficiently low, and the correlation strength is sufficiently high. Preferential adsorption of solvent enhances the effect and shifts the transition to higher concentrations where RTILs are typically used. Near the transition at finite potential, the capacitance becomes very large.

In Fig. 9, the surface charge, differential capacitance, and energy storage are plotted as a function of the applied potential for a solvophilic electrode. We see that the spike in capacitance (Fig. 9b) at a finite potential difference leads to a sudden rapid increase in the energy storage (Fig. 9c), which naturally comes from the definition of energy storage given in eqn (16). Previous studies that focused on ion adsorption into nanopores have shown a similar increase in energy storage when using *ionophobic* electrodes.[57–60] Generally, wider peaks in capacitance shifted to larger applied potentials lead to more energy storage. Also, we still observe the trend that more dilute RTILs store more energy when charged to relatively higher potentials. This is due to the higher differential capacitance at higher potential. In the high potential limit we still observe the expected $\Delta V^{-1/2}$ behavior.[15]

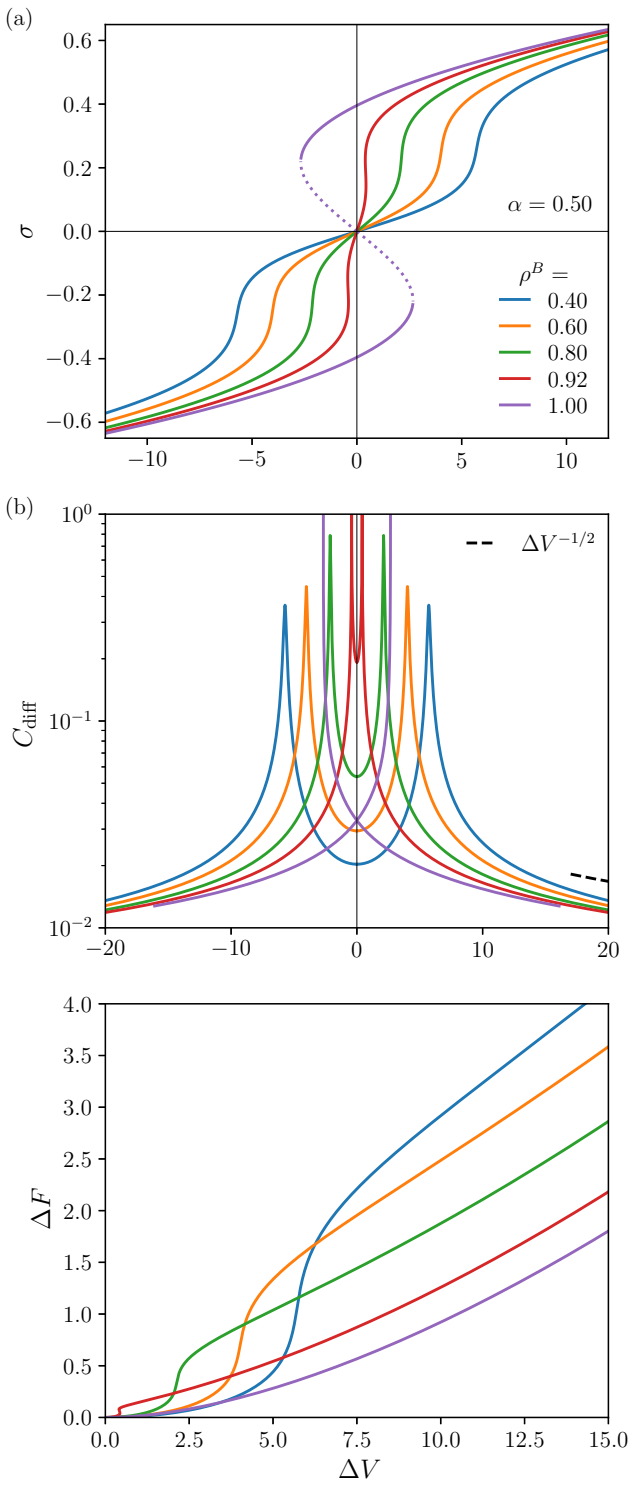

Fig. 9 (a) σ vs ΔV plotted for a RTILs with varying dilution, $\alpha = 0.50$, and a solvophilic electrode ($\Delta h = -5.0$). The dashed portion of $\rho_B = 1.0$ (purple) curve is the region of instability. (b) C_{diff} vs ΔV plotted for RTILs with varying dilution on semi-log scale and (c) energy storage ΔF vs ΔV for diluted RTILs. The legend in (a) applies to (b) and (c) as well.

Conclusions

The RTIL concentration is a powerful design handle for EDLCs. While some factors such as the correlation strength and length, or the chemical nature of the electrode can be difficult and expensive to vary, concentration is very simple, yet effective for tuning capacitance and energy storage. For example, the hysteresis in RTILs due to strong correlation effects[18,32–34] can be mitigated by dilution. Addition of a neutral solvent works to separate ions and decrease the effect of the short-ranged correlations. By diluting, one can modulate the proximity to SSCS to fine tune and bolster the capacitance.

When a neutral solvent is added, there is also a rich phase behavior similar to that of the well known BC (or BEG) model. At high concentrations SSCS is a second-order transition at the mean-field level, whereas at low concentrations SSCS is a first-order transition. The transition from second-order to first-order occurs at the tricritical point which exists at a bulk ion volume fraction of $\rho^B = 1/3$, the same volume fraction of the tricritical point in the BC model. This volume fraction also corresponds to the transition between bell and camel-shaped capacitance curves as discovered by Kornyshev.[15]

If the electrode shows preference for the solvent, this further reduces the effect of SSCS, pushing the transition to finite potentials where ions are attracted to the charged electrodes. This preference for solvent can lead to a surface charge transition at a *finite potential* where the surface charge rapidly increases (or even jumps), and the electric double layer is flooded with ions to counteract the charge. The rapid increase in surface charge is favorable when continuous due to the increased capacitance and energy storage. However, a jump in surface charge could lead to unfavorable hysteresis in charging and discharging similarly to neat RTILs.[32,33] We achieved a significant increase in energy storage without considering asymmetric adsorption of the ions as in Ref. 18. The presence of solvent allows for the phase transition at finite potential, which could not occur in a neat RTIL without introducing asymmetry.

Based on these results, the ideal charging behavior is achieved when the concentration and correlation strength are such that the system is near but not above the critical concentration for a finite potential surface phase transition. The solvent choice and concentration serve as easy handles for modulating the phase behavior and maximizing the capacitance.

While we only apply a mean-field treatment of RTILs with a phenomenological correction for ion–ion correlations, similar models have been used to predict qualitative behavior observed in experiments.[15,17,18,30,31] The lattice-gas-like model used here is not able to incorporate any ion packing effects. Future works should consider more sophisticated theories that account for liquid structure such as classical density functional theory (cDFT) and weighted density theories. Size asymmetry can be incorporated into future studies where the solvent, cation, and anion can be treated explicitly with different sizes. Size asymmetry has been previously considered using Monte Carlo, cDFT,[61] MFT without ion–ion correlations,[41] and continuum theory,[62] but there has not been work looking at the phase behavior and energy storage

performance in asymmetric systems. Size asymmetry will shift the peak in the capacitance from zero potential in a similar manner to preferential adsorption, enhancing the energy storage from charging. It is also of interest to look at RTIL behavior in curved environments. Some studies are already looking at the EDL structure for RTILs near curved surfaces[5,63,64], but there is still work to be done specifically in confined systems with curvature. With the advent of wearable technology, supercapacitors are being targeted for power delivery in flexible electronics, where electrode curvature is of utmost importance.[65] Much work can be done even at the mean-field level. Future works should incorporate the effects explored in this work such as dilution, correlations, and non-electrostatic interactions, while including additional effects such as size asymmetry, curvature, and confinement.

Conflicts of interest

There are no conflicts to declare.

Appendix A: Nomenclature

Abbreviations

RTIL	Room temperature ionic liquid
EDLC	Electric double layer capacitor
SSCS	Spontaneous surface charge separation
SC	Supercapacitor
PD	Power density
ED	Energy density
AN	Acetonitrile
PC	Propylene carbonate
IL	Ionic liquid
EDL	Electric double layer
BSK	Bazant–Storey–Kornyshev
MFT	Mean-field theory
CW	Chao–Wang
BC	Blume–Capel
BEG	Blume–Emery–Griffiths
cDFT	Classical Density Functional Theory

Symbols

C	Capacitance
V	Cell potential
γ	Compacity
U	Potential energy
r	Particle distance
ℓ_c	Correlation length
λ_D	Debye length
α	Correlation strength
$\alpha_{s,c}$	Surface critical correlation strength
v	Molecular volume
b	Molecular size, $v = b^3$
ϕ_i^B	Bulk volume fraction of species i
c_i^B	Bulk number density of species i
ε	Dielectric constant
$\mathbf{r}$	Vector position
β	Inverse temperature, $1/k_BT$
k_B	Boltzmann constant
T	Temperature
Ω	Grand free energy
λ_0	Nominal screening length
μ_i	Chemical potential of species i
ε_r	Relative permittivity
ϕ	Local charge density
ε_0	Vacuum permittivity
e	Elementary charge
z	Coordinate normal to electrode
$\mathbf{r}_{\|\|}$	2-dimensional position parallel to electrode
χ	Flory-chi parameter
L	Electrode separation
Ψ	Electrostatic potential
ψ	Nondimensional electrostatic potential, $\beta e\Psi$
A	Electrode surface area
σ	Surface charge density
U	Yukawa potential
H_i	Preferential adsorption potential
h_i	Preferential adsorption strength of species i
Δh_i	Relative adsorption strength of species i (relative to solvent)
Δh	Symmetric relative adsorption strength
Y	Yukawa field

μ_i^B	Bulk chemical potenital of species i
μ	Ion chemical potential in symmetric IL
ΔV	Electrode potential difference
$\psi_{\pm L/2}$	Electrostatic potential on electrode
C_{diff}	Differential capacitance
ΔF	Stored energy per surface area
ρ_B	Bulk ion volume fraction
$\alpha_{sc,neat}$	Surface critical correlation strength in neat RTIL
$\alpha_{sc,dilute}$	Surface critical correlation strength in dilute RTIL
H	Hamiltonian
N	Particle number
$\mathbf{s}$	Spin configuration
s_i	Spin on particle i
μ_A, μ_B	Chemical potential of particle type A, and B
J	Ferromagnetic interaction strength
$\Delta\mu$	Chemical potential difference between A and B
m	Relative magnetisation order parameter
x	Mole fraction of type A
G	Variational free energy
S	Entropy

Acknowledgements

S.V. is supported by the U.S. Department of Energy, Office of Science, Office of Advanced Scientific Computing Research, Department of Energy Computational Science Graduate Fellowship under Award Number DE-SC0022158. Z.-G. W. acknowledges financial support from the Hong Kong Quantum AI Lab Ltd.

Notes and references

1 C. Zhong, Y. Deng, W. Hu, J. Qiao, L. Zhang and J. Zhang, *Chem. Soc. Rev.*, 2015, **44**, 7484–7539.
2 W. G. Pell and B. E. Conway, *Journal of Power Sources*, 1996, **63**, 255–266.
3 A. Muzaffar, M. B. Ahamed, K. Deshmukh and J. Thirumalai, *Renewable and Sustainable Energy Reviews*, 2019, **101**, 123–145.
4 P. Sharma and T. S. Bhatti, *Energy Conversion and Management*, 2010, **51**, 2901–2912.
5 F. Béguin, V. Presser, A. Balducci and E. Frackowiak, *Adv. Mater.*, 2014, **26**, 2219–2251.
6 A. Balducci, *Journal of Power Sources*, 2016, **326**, 534–540.
7 P. Simon and Y. Gogotsi, *Acc. Chem. Res.*, 2013, **46**, 1094–1103.
8 K. L. Van Aken, M. Beidaghi and Y. Gogotsi, *Angew. Chem. Int. Ed.*, 2015, **54**, 4806–4809.
9 M. P. S. Mousavi, B. E. Wilson, S. Kashefolgheta, E. L. Anderson, S. He, P. Bühlmann and A. Stein, *ACS Appl. Mater. Interfaces*, 2016, **8**, 3396–3406.
10 M. Armand, F. Endres, D. R. MacFarlane, H. Ohno and B. Scrosati, *Nature Mater*, 2009, **8**, 621–629.
11 T. Sato, G. Masuda and K. Takagi, *Electrochimica Acta*, 2004, **49**, 3603–3611.
12 E. Frackowiak, G. Lota and J. Pernak, *Appl. Phys. Lett.*, 2005, **86**, 164104.
13 H. Helmholtz, *Ann. Phys. Chem.*, 1853, **165**, 211–233.
14 M. Gouy, *J. Phys. Theor. Appl.*, 1910, **9**, 457–468.
15 A. A. Kornyshev, *J. Phys. Chem. B*, 2007, **111**, 5545–5557.
16 M. Z. Bazant, B. D. Storey and A. A. Kornyshev, *Phys. Rev. Lett.*, 2011, **106**, 046102.
17 D. L. Z. Caetano, G. V. Bossa, V. M. de Oliveira, M. A. Brown, S. J. de Carvalho and S. May, *Phys. Chem. Chem. Phys.*, 2016, **18**, 27796–27807.
18 H. Chao and Z.-G. Wang, *J. Phys. Chem. Lett.*, 2020, **11**, 1767–1772.
19 D. di Caprio, Z. Borkowska and J. Stafiej, *Journal of Electroanalytical Chemistry*, 2003, **540**, 17–23.
20 D. di Caprio, Z. Borkowska and J. Stafiej, *Journal of Electroanalytical Chemistry*, 2004, **572**, 51–59.
21 I. Borukhov, D. Andelman and H. Orland, *Phys. Rev. Lett.*, 1997, **79**, 435–438.
22 R. Netz and H. Orland, *Eur. Phys. J. E*, 2000, **1**, 203.
23 D. B. Levin and R. Chahine, *International Journal of Hydrogen Energy*, 2010, **35**, 4962–4969.
24 B. Skinner, M. S. Loth and B. I. Shklovskii, *Phys. Rev. Lett.*, 2010, **104**, 128302.
25 P. Reichert, K. S. Kjær, T. B. v. Driel, J. Mars, J. W. Ochsmann, D. Pontoni, M. Deutsch, M. M. Nielsen and M. Mezger, *Faraday Discuss.*, 2017, **206**, 141–157.
26 R. M. Lynden-Bell, A. I. Frolov and M. V. Fedorov, *Phys. Chem. Chem. Phys.*, 2012, **14**, 2693.
27 Y. Levin, *Rep. Prog. Phys.*, 2002, **65**, 1577–1632.
28 C. D. Santangelo, *Phys. Rev. E*, 2006, **73**, 041512.
29 A. A. Lee, S. Kondrat, D. Vella and A. Goriely, *Phys. Rev. Lett.*, 2015, **115**, 106101.
30 G. V. Bossa and S. May, *Phys. Rev. Research*, 2020, **2**, 032040.
31 Z. Lian, H. Chao and Z.-G. Wang, *ACS Nano*, 2021, 11724–11733.
32 W. Zhou, S. Inoue, T. Iwahashi, K. Kanai, K. Seki, T. Miyamae, D. Kim, Y. Katayama and Y. Ouchi, *Electrochemistry Communications*, 2010, **12**, 672–675.
33 M. Drüschler, B. Huber, S. Passerini and B. Roling, *J. Phys. Chem. C*, 2010, **114**, 3614–3617.
34 D. T. Limmer, *Phys. Rev. Lett.*, 2015, **115**, 256102.
35 B. B. Ye and Z.-G. Wang, *Phys. Chem. Chem. Phys.*, 2022, **24**, 11573–11584.

36 D. J. Bozym, B. Uralcan, D. T. Limmer, M. A. Pope, N. J. Szamreta, P. G. Debenedetti and I. A. Aksay, *J. Phys. Chem. Lett.*, 2015, **6**, 2644–2648.

37 R.-S. Kühnel, N. Böckenfeld, S. Passerini, M. Winter and A. Balducci, *Electrochimica Acta*, 2011, **56**, 4092–4099.

38 V. Ruiz, C. Blanco, E. Raymundo-Piñero, V. Khomenko, F. Béguin and R. Santamaría, *Electrochimica Acta*, 2007, **52**, 4969–4973.

39 A. Lewandowski, A. Olejniczak, M. Galinski and I. Stepniak, *Journal of Power Sources*, 2010, **195**, 5814–5819.

40 J. Bikerman, *Philos. Mag.*, 1942, **33**, 384–397.

41 Y. Han, S. Huang and T. Yan, *J. Phys.: Condens. Matter*, 2014, **26**, 284103.

42 J. P. de Souza and M. Z. Bazant, *J. Phys. Chem. C*, 2020, **124**, 11414–11421.

43 Z. A. H. Goodwin, G. Feng and A. A. Kornyshev, *Electrochimica Acta*, 2017, **225**, 190–197.

44 Z.-G. Wang, *J. Theor. Comput. Chem.*, 2008, **07**, 397–419.

45 G. H. Fredrickson, *The equilibrium theory of inhomogeneous polymers*, Clarendon Press ; Oxford University Press, Oxford : New York, 2006.

46 C. Wakai, A. Oleinikova, M. Ott and H. Weingärtner, *J. Phys. Chem. B*, 2005, **109**, 17028–17030.

47 G. M. Torrie and J. P. Valleau, *J. Chem. Phys.*, 1980, **73**, 5807–5816.

48 S. A. Brazovski?, *30 Years of the Landau Institute ? Selected Papers*, WORLD SCIENTIFIC, 1996, vol. Volume 11, pp. 109–113.

49 M. Blume, *Phys. Rev.*, 1966, **141**, 517–524.

50 H. W. Capel, *Physica*, 1966, **32**, 966–988.

51 M. Blume, V. J. Emery and R. B. Griffiths, *Phys. Rev. A*, 1971, **4**, 1071–1077.

52 L. Blum, *Molecular Physics*, 1975, **30**, 1529–1535.

53 M. Dudka, S. Kondrat, A. Kornyshev and G. Oshanin, *J. Phys.: Condens. Matter*, 2016, **28**, 464007.

54 Y. Groda, M. Dudka, A. A. Kornyshev, G. Oshanin and S. Kondrat, *J. Phys. Chem. C*, 2021, **125**, 4968–4976.

55 S. May, *Current Opinion in Electrochemistry*, 2019, **13**, 125–131.

56 C. Cruz, A. Ciach, E. Lomba and S. Kondrat, *J. Phys. Chem. C*, 2019, **123**, 1596–1601.

57 A. A. Lee, S. Kondrat and A. A. Kornyshev, *Phys. Rev. Lett.*, 2014, **113**, 048701.

58 S. Kondrat and A. A. Kornyshev, *Nanoscale Horiz.*, 2015, **1**, 45–52.

59 A. A. Lee, D. Vella, A. Goriely and S. Kondrat, *Phys. Rev. X*, 2016, **6**, 021034.

60 C. Lian, H. Liu, D. Henderson and J. Wu, *J. Phys.: Condens. Matter*, 2016, **28**, 414005.

61 S. Lamperski, J. Sosnowska, L. B. Bhuiyan and D. Henderson, *The Journal of Chemical Physics*, 2014, **140**, 014704.

62 J. P. de Souza, K. Pivnic, M. Z. Bazant, M. Urbakh and A. A. Kornyshev, *J. Phys. Chem. B*, 2022, **126**, 1242–1253.

63 G. Feng, D.-e. Jiang and P. T. Cummings, *J. Chem. Theory Comput.*, 2012, **8**, 1058–1063.

64 D. L. Z. Caetano, S. J. de Carvalho, G. V. Bossa and S. May, *Phys. Rev. E*, 2021, **104**, 034609.

65 Y. Liu, C. Lu, S. Twigg, M. Ghaffari, J. Lin, N. Winograd and Q. M. Zhang, *Sci Rep*, 2013, **3**, 973.